Chemical Engineering Journal 512 (2025) 162535

Contents lists available at ScienceDirect

Chemical Engineering Journal

journal homepage: www.elsevier.com/locate/cej

Elucidating of moisture-induced degradation and rehealing of alluaudite $Na_{2+2x}Fe_{2-x}(SO_4)_3$ cathode for Sodium-Ion batteries

Jiayue Wu, Xing Chen, Jing Zeng *, Jinbao Zhao *

College of Chemistry and Chemical Engineering, State-Province Joint Engineering Laboratory of Power Source Technology for New Energy Vehicle, State Key Laboratory of Physical Chemistry of Solid Surfaces, Engineering Research Center of Electrochemical Technology, Ministry of Education, Collaborative Innovation Center of Chemistry for Energy Materials, Xiamen University, Xiamen 361005, PR China

ARTICLE INFO

Keywords:
$Na_{2+2x}Fe_{2-x}(SO_4)_3$
Cathode
Moisture-induced degradation
Capacity regeneration
Sodium-ion batteries

ABSTRACT

Polyanion-type iron-based sulfates are promising candidates for cathode in sodium-ion batteries due to the cost-effectiveness. However, the material exhibits a high sensitivity to humidity, which significantly increases the costs associated with cell fabrication. Therefore, it's critical for the industrial application to understand the humidity-induced degradation mechanism and develop regeneration strategies. In this study, $Na_{2.67}Fe_{1.67}(SO_4)_3$ (NFS) exhibiting an outstanding capacity retention of 77.8 % after 6000 cycles, is used as the model to systematically investigate the intrinsic causes of degradation upon exposure to moisture. Specifically, water ingress and the strong Coulombic repulsion between Fe-Fe induce the decoupling of the $[Fe_2O_{10}]$ dimer, causing the transformation into bloedite-type $Na_2Fe(SO_4)_2{\cdot}4H_2O$. The π-contributing orbital interaction between O of water and Fe, along with the hydrogen-bonding network formed between H in water and the lattice O, confers additional structural stability to the hydrate. Theoretical calculations and enthalpy measurements indicate that the hydration reaction is thermodynamically spontaneous, with the Gibbs free energy change of −0.91 eV and the enthalpy change of −22.083 kJ/mol. After two days of exposure to 50 % humidity, the capacity degrades to approximately 83.5 % and a secondary heating strategy is developed to restore the fully degraded NFS to its original crystal structure and recover up to 94 % of the initial capacity. This study provides comprehensive insights into the causes of air instability in NFS and proposes an effective strategy for capacity regeneration.

1. Introduction

Large-scale energy storage is essential for transitioning towards a more sustainable and resilient energy future, as it enables improved integration of renewable energy for reliable and cost-effective power supply [1,2]. Lithium-ion batteries (LIBs), featuring the outstanding energy density and exceptional cycling lifetime, are applicable to contemporary portable applications involving electronics and electric vehicles [3,4]. Unfortunately, due to their prohibitive expense, restricted availability of ingredients, and security concerns, they don't facilitate large-scale energy storage, where cost-effectiveness and safety are prioritized [5,6]. In this regard, sodium-ion batteries (SIBs) have attracted significant attention owing to their abundant primary resources and competitive price [7].

Cathode materials dominate in SIBs because they intimately correlate with the battery energy density, cycling life and efficiency [8]. High-performance cathode materials primarily comprise layered transition metal oxides, Prussian blue analogs and polyanionic compounds [9]. Among them, polyanionic cathodes ($Na_xM_y[(X_aO_b)_z]$, M = Fe, V, Mn, Co, etc.; X = P, S, Si, etc.) possess the benefit of a rigid framework structure attributing to outstanding stability [10,11]. The richer electronegativity of the X in the anion produces a stronger induced effect conducing to a higher redox potential, thus the sulfate cathode presents a considerable competitive advantage as a consequence of the impressive electronegativity of SO_4^{2-} [12,13]. $Na_{2+2x}Fe_{2-x}(SO_4)_3$ reported by Yamada in 2014 exhibited a higher redox potential of 3.8 V (versus Na^+/Na), providing a higher theoretical energy density of 456 Wh/kg than that of NFPP ($Na_4Fe_3(PO_4)_2(P_2O_7)$, 399.9 Wh/kg) and NVP ($Na_3V_2(PO_4)_3$, 360 Wh/kg) [14–17]. Additionally, the low cost of raw materials and simple synthesis process of $Na_{2+2x}Fe_{2-x}(SO_4)_3$ make it a cost-effective option for SIBs cathodes.

Unfortunately, owing to the comparable Lewis basicity of oxygen atoms in SO_4^{2-} and H_2O, sulfate-based cathode materials universally exhibit moisture sensitivity [18,19]. Ambient humidity must be

* Corresponding authors.
E-mail addresses: zengjing@xmu.edu.cn (J. Zeng), jbzhao@xmu.edu.cn (J. Zhao).

https://doi.org/10.1016/j.cej.2025.162535
Received 4 February 2025; Received in revised form 31 March 2025; Accepted 9 April 2025
Available online 11 April 2025

stringently controlled during material storage and battery cell preparation, leading to significantly increased costs. Therefore, it is a critical issue for practical applications to elucidate the moisture degradation mechanism and achieve capacity rehealing after degradation of materials. The phenomenon of moisture degradation in sulfate-based cathodes has been reported in LIBs. Chen et al. demonstrated that tavorite-type $LiFeSO_4F$ underwent complete transformation into $FeSO_4{\cdot}nH_2O$ (n = 1, 4, 7) and LiF when exposed to humidity exceeding 62 % [20]. After aging in high-moisture environments, $LiFeSO_4F$ formed an electrochemically active (Li)$FeSO_4OH$ phase without F^- *in situ* during battery circulation. Barpanda et al. synthesized two polymorphs of $Li_2Ni(SO_4)_2$, both of which evolved into $NiSO_4{\cdot}6H_2O$ and $Li_2SO_4{\cdot}H_2O$ upon exposure to atmosphere for two weeks [19]. The majority of sulphate-based insertion materials form the respective hydrated precursors ($FeSO_4{\cdot}nH_2O$, n = 1/4/7) upon moisture erosion. With regard to $Na_{2+2x}Fe_{2-x}(SO_4)_3$, reports indicated that a hydrated phase, $Na_2Fe(SO_4)_2{\cdot}4H_2O$, was inclined to develop upon moisture, but its intrinsic causes and corresponding changes in electrochemical performance have not yet to be elucidated [21–23]. More importantly, the restoration of capacity in degraded materials has yet to be resolved.

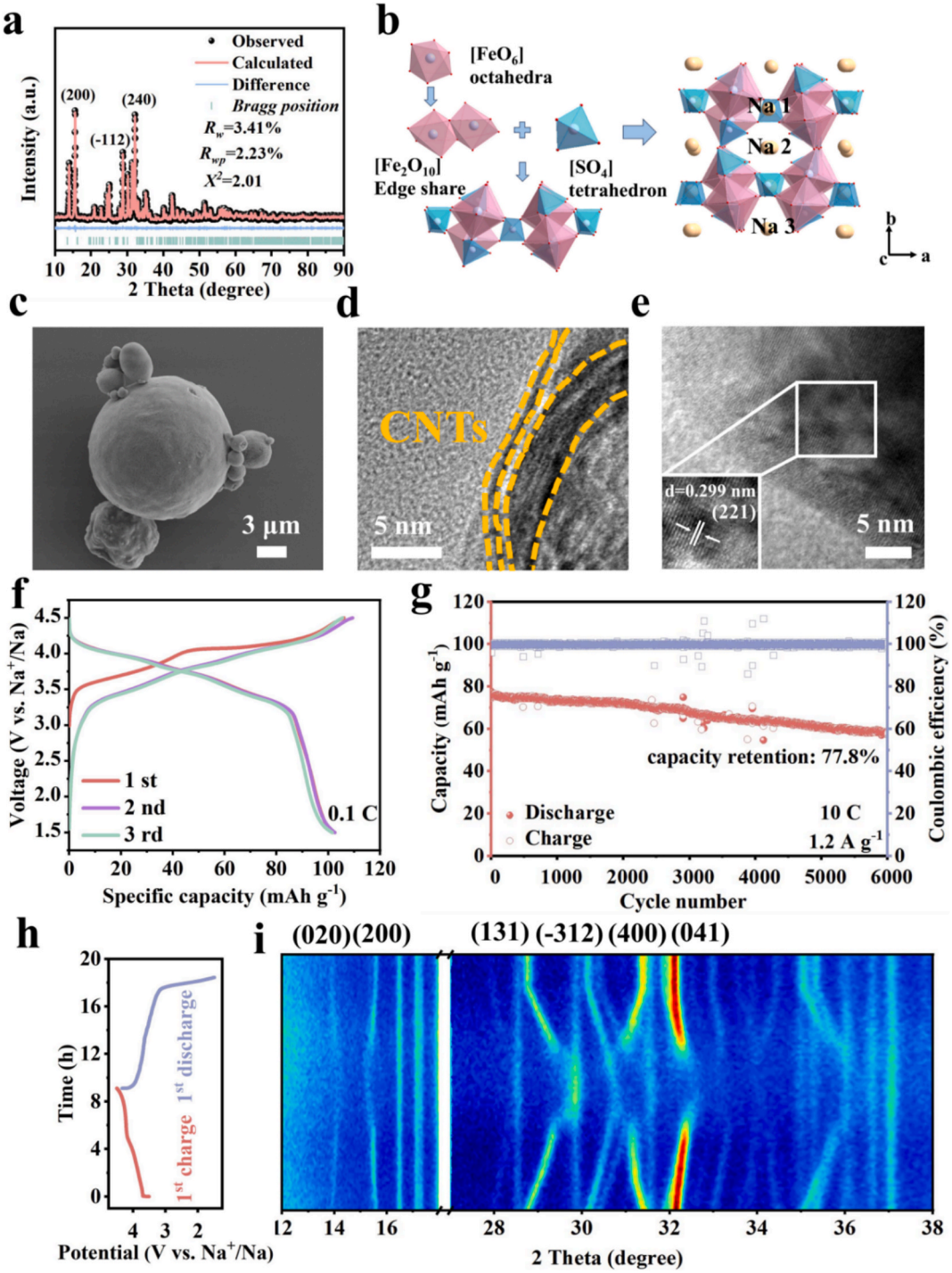

Fig. 1. A) Rietveld refinement XRD pattern and b) crystal structure of NFS. c) Enlarged SEM image of NFS sphere. d) TEM image of CNTs network around the NFS surface. e) HRTEM image showing the lattice fringes of NFS. f) Charge-discharge curves for the initial three cycles and g) long-cycling performance at 10C of NFS. h) The charge–discharge curves of the first cycle for *in situ* XRD tests. i) Contour map of *in situ* XRD results.

Here, $Na_{2.67}Fe_{1.67}(SO_4)_3$ (NFS) with an outstanding electrochemical performance of 103 mAh/g is used as the model to investigate its degradation process upon certain humidity conditions. Experimental results indicate that at 50 % humidity, alluaudite-type $Na_{2+2x}Fe_{2-x}(SO_4)_3$ gradually transforms into bloedite-type $Na_2Fe(SO_4)_2{\cdot}4H_2O$, and $FeSO_4{\cdot}7H_2O$ appears at 80 % humidity. Thermodynamic cycle calculations show that the enthalpy change for this hydration process is –22.083 kJ/mol and theoretical calculations suggest that the Gibbs free energy (ΔG) of the reaction is −0.91 eV, indicating that alluaudite spontaneously converses the more stable bloedite under humidity-induced conditions. The π-contributing orbital interaction between the oxygen of water and Fe, along with the hydrogen-bonding network formed between the hydrogen in water with lattice oxygen, imparts additional structural stability to the hydrate, leading to a reduction in the overall system energy after hydration. X-ray diffraction (XRD) refinement and electrochemical performance test results indicate that the content of the hydrated phase increases linearly to 31.7 % after 48 h of storage at 50 % humidity and the discharge capacity correspondingly degrades to approximately 83.5 %, which is caused by the poor sodium storage capability of the hydrated phase and decreased conductivity. Since alluaudite and bloedite undergo reverse reactions, a simple strategy is proposed to restore the initial crystal structure of the completely degraded material by heating to remove the crystal water. The re-heat material recovers 94 % of the initial specific capacity, with some capacity loss accounted for the irreversible loss of active electrochemical pairs and the reduced electronic conductivity owing to the disruption of the conductive network by water removal.

2. Results and discussion

NFS is produced using a spray-drying synthesis route illustrated in **Fig. S1** and the off-stoichiometric NFS with a Na/Fe ratio of 1.6 is determined to be optimal for further investigation based on XRD and electrochemical performance tests results (**Fig. S2a-c**). To obtain finer structural information, Rietveld refinement is performed and the results confirm that the as-synthesized NFS exhibits outstanding purity, belonging to the C2/c space group with a monoclinic crystal system (Fig. 1**a**). The refined lattice parameters are a = 12.6592 Å, b = 12.7792 Å, c = 6.51907 Å, β = 115.545°, and V = 951.5038 $Å^3$, which are in agreement with values reported in the literature (**Table S1**) [24–26]. This yields a three-dimensional structural framework where two $[FeO_6]$ octahedra share an edge to assemble $[Fe_2O_{10}]$ dimers, which are alternately attached with $[SO_4]$ tetrahedra at a co-oxygen atom, creating channels along the c-axis for Na^+ insertion and extraction (Fig. 1**b**). ICP-OES analysis determines the atomic ratio of Na:Fe:S in NFS to be approximately 2.67:1.67:3 (**Table S2**), and elemental analysis reveals a carbon content of 2.05 wt% in NFS, which enable the confirmation of the material chemical composition. SEM and TEM reveal the NFS particles are spherical with an average diameter of 3–5 μm (Fig. 1**c and Fig. S3a-c**). High-resolution TEM (HRTEM) image shown in Fig. 1**d** indicates a well-defined CNTs visible around the NFS material, forming a long-range conductive network on the surface, significantly improving the electronic conductivity. The lattice fringe of 0.299 nm observed in Fig. 1**e** corresponds to the (221) crystal plane in NFS.

The electrochemical behavior of NFS is further studied in detail. The charge–discharge curves of NFS for the initial three cycles are illustrated as Fig. 1**f**, manifesting an operating voltage of approximately 3.8 V, which can provide a relatively high theoretical energy density of 456 Wh/kg. The shape of the first charge curve differs significantly from the subsequent ones consistent with the features observed in the CV curves (**Fig. S4a**), which is resulted from the structural rearrangement during the first charging process [27]. Significantly, NFS exhibits a superior long-cycling performance, with a capacity retention of 77.8 % after 6000 cycles at a rate of 10 C and the exceptional rate performance with 71.36 mAh/g at 20 C (Fig. 1**g and Fig. S4b**). Due to the long-range conductive network provided by CNTs, the NFS with CNTs exhibits an increased specific capacity of 103 mAh/g, with the capacity contribution of the CNTs being negligible (**Fig. S4g-h**). And the material demonstrates stable cycling performance at 60 °C, indicating the structural stability (**Fig. S4i**). This is attributed to the rapid electron and ion mobility, as confirmed by GITT and variable-rate CV measurements (**Fig. S4c-f**) [28]. Additionally, *in situ* XRD of NFS is subsequently performed to investigate the evolution of its crystal structure during the first charge–discharge cycle (Fig. 1**h-i**). All characteristic peaks show reversible shifts during the charge–discharge process, indicating that the material maintains a stable structural framework.

Despite the high electronegativity of SO_4^{2-} in NFS initiates high voltage activity, the Lewis basicity of the oxygen atoms in SO_4^{2-} is equivalent to that in water, which makes sulfates intrinsically hypersensitive to moisture [29]. Therefore, it is imperative to investigate the air stability and deterioration mechanism of NFS. The NFS is subjected to Constant Temperature and Humidity Test Chamber with 50 % humidity at 25 ℃ to explore the moisture-induced deterioration progression. After 24 h of storage, an appearance of the impurity peaks is distinctly observable at 19.5° and 27.1° in the XRD pattern, corresponding to the hydrated phase $Na_2Fe(SO_4)_2{\cdot}4H_2O$ (Fig. 2**a**). As time progresses, the intensity of the peaks pertaining to the alluaudite-type phase diminishes, while the peaks intensity of the hydrated derivatives progressively intensifies (**Fig. S5**). This indicates a proclivity of NFS from the alluaudite-type $Na_{2+2x}Fe_{2-x}(SO_4)_3$ to bloedite-type $Na_2Fe(SO_4)_2{\cdot}4H_2O$ upon the moisture. In order to accelerate the study of the moisture-induced phase transition, a high-humidity environment is employed to store NFS for expedited deterioration (80 % humidity). A complete conversion occurs in the refined XRD patterns into a mixture of $Na_2Fe(SO_4)_2{\cdot}4H_2O$ and $FeSO_4{\cdot}7H_2O$, with phase proportions of 86.34 % and 13.66 %, respectively (**Fig. S6a-b and Table S3-S4**).

Above-mentioned findings demonstrate that the water absorption process of the material leads to a phase transition from the alluaudite to the bloedite and the schematic diagram of the crystal structure transformation between the two phases is shown in Fig. 2**b**. Upon water absorption, due to the ingress of water molecules and the large Coulomb repulsive force between Fe and Fe, the structural units of material alter from alternating $[Fe_2O_{10}]$ dimers and $[SO_4]$ to $[FeO_6]$ octahedra connected to two $[SO_4]$ tetrahedra and four H_2O. Fig. 2**c-f** illustrate the XRD Rietveld refinement of NFS after various storage time, all yielding satisfactory fits. The XRD refinement results indicate that with increasing storage time, the Fe-Fe bond distance increases, suggesting the decoupling of the $[Fe_2O_{10}]$ dimer structure (**Fig. S7**). Through XRD refinement, specific variations in the lattice parameters and phase content of NFS with storage time can be ascertained (**Table S5-S12**). The lattice parameters a, b, c, and V of $Na_{2+2x}Fe_{2-x}(SO_4)_3$ gradually follow a continuous increase with time, as water intrusion into the material pores causes expansion in all axial directions (Fig. 2**g**). In contrast, the lattice parameters a, b, c, and V of the impurity phase $Na_2Fe(SO_4)_2{\cdot}4H_2O$ gradually decrease over time due to the tighter rearrangement of atoms within the hydrated crystal, which results in phase stabilization (Fig. 2**h**). The bar chart in Fig. 2**i** suggests the time-dependent changes in the phase content of the two phases. By fitting the phase content to storage time, we observe an ideal primary linear correlation, which is instrumental in predicting the air stability and lifespan of NFS over storage time at 50 % humidity.

To further investigate the intrinsic causes for moisture-induced degradation of NFS material, ΔG for the reaction of NFS with water is calculated using density functional theory (DFT). The optimized structure of the NFS model is shown in **Fig. S8a**, with the calculated band gap of 1.775 eV (**Fig. S8b**). The process of water entering the material lattice and adsorbing at Fe-centered sites is depicted in Fig. 3**a**. In this process, the interaction between the π-electrons on O atoms of the water and the empty or partially filled 3d orbitals on Fe^{2+} results in the formation of the coordination bonds, thereby enhancing the stability of the complex (Fig. 3**b**). Furthermore, the H atoms of the water interact with the O atoms in the lattice via hydrogen bonds, which provides additional

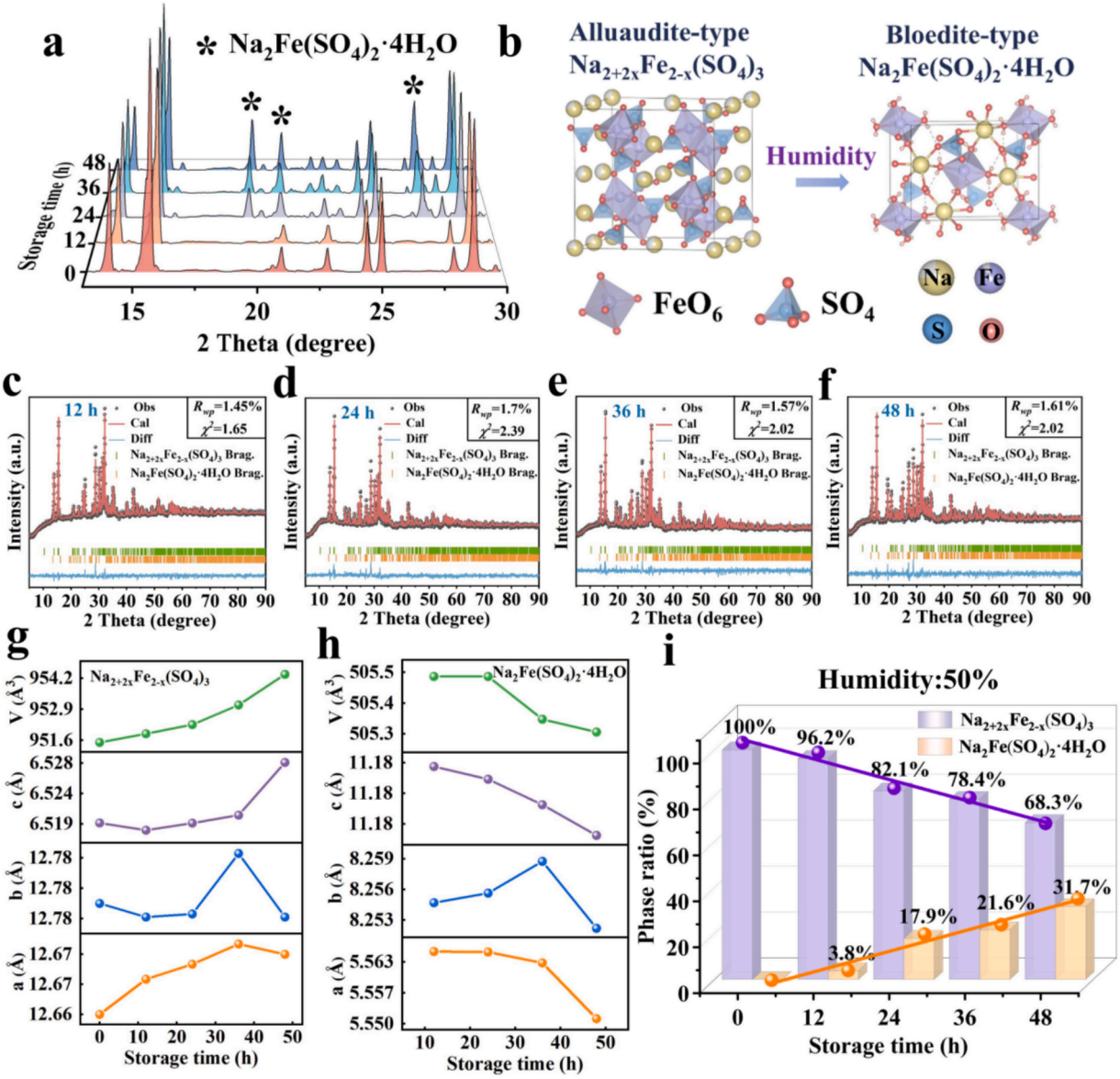

Fig. 2. A) xrd patterns changes of nfs at 50 % humidity over time. b) Crystal phase transition after water absorption. c-f) Refined XRD patterns of NFS for various storage time at 50 % humidity. g) Variation of lattice parameters of $Na_{2+2x}Fe_{2-x}(SO_4)_3$ with storage time. h) Changes of lattice parameters of $Na_2Fe(SO_4)_2{\cdot}4H_2O$ with storage time. i) Comparison of phase content of $Na_{2+2x}Fe_{2-x}(SO_4)_3$ and $Na_2Fe(SO_4)_2{\cdot}4H_2O$ as time progresses and linear fitting of phase content with time.

structural stability to the material (Fig. 3**c**). The ΔG for the reaction between NFS and H_2O is calculated to be −0.91 eV, indicating that the process is spontaneous reaction. The results of the above calculations consistently illustrate that NFS exhibits a strong affinity for water and is more likely to form the hydrate.

In addition, the enthalpies of formation for NFS and degraded NFS are experimentally measured using isothermal acid solution calorimetry in order to compare the thermodynamic stability of $Na_{2+2x}Fe_{2-x}(SO_4)_3$ and $Na_2Fe(SO_4)_2{\cdot}4H_2O$ [30,31]. The schematic diagram and principle of the instrument used are shown in Fig. 3**d**. By controlling the balance between the sample cell and the reference cell, the power generated by the reaction is quantitatively calculated, and the enthalpy change of the reaction is obtained by integrating the power over time. The calorimetric data for $Na_{2+2x}Fe_{2-x}(SO_4)_3$ and $Na_2Fe(SO_4)_2{\cdot}4H_2O$ are shown in Table 1. The power changes of the reactants and products dissolved in 5 M HCl are recorded (**Fig. S9a-d**), and the dissolution enthalpies (ΔH_{ds}) obtained from the integration of power are listed in Table 1. The dissolution enthalpy of $Na_{2+2x}Fe_{2-x}(SO_4)_3$ is 2.633 kJ/mol, while that of $Na_2Fe(SO_4)_2{\cdot}4H_2O$ is 31.87 kJ/mol. Using the thermodynamic cycle in **Table S13**, we calculate the enthalpies of formation (ΔH_f) for these two products using the Na_2SO_4-$FeSO_4$ binary constituent system as the reactants. The formation enthalpy of $Na_{2+2x}Fe_{2-x}(SO_4)_3$ is −8.997 kJ/mol, while that of $Na_2Fe(SO_4)_2{\cdot}4H_2O$ is −31.08 kJ/mol, both of which are exothermic and spontaneous reactions. The enthalpy of the reaction between alluaudite and water to form bloedite is further calculated to be –22.083 kJ/mol using the thermodynamic cycle in Fig. 3**e**. The exothermic spontaneous reaction drives the formation of the bloedite phase and thermodynamically justifies the argument that $Na_{2+2x}Fe_{2-x}(SO_4)_3$ undergoes a moisture-induced phase transition spontaneously.

The FT-IR, Raman, and SEM characterizations are performed to investigate the degradation process of NFS. After 48 h storage, a significant hydroxyl peak at about 3450 cm^{-1} associated with water is prominently observed in the FT-IR spectrum (Fig. 4**a**) [32]. A variation at a lower wavenumber of 594 cm^{-1} assigned to the Fe-O peak in the FT-IR spectra is noticeable from a split peak to a single peak of NFS stored in a high-humidity environment (**Fig. S10a**) [33–35]. This is due to the weakened interaction of [Fe_2O_{10}] dimers transforming into [FeO_6] octahedra. The Raman spectra exhibit a conspicuous increase in the I_D/

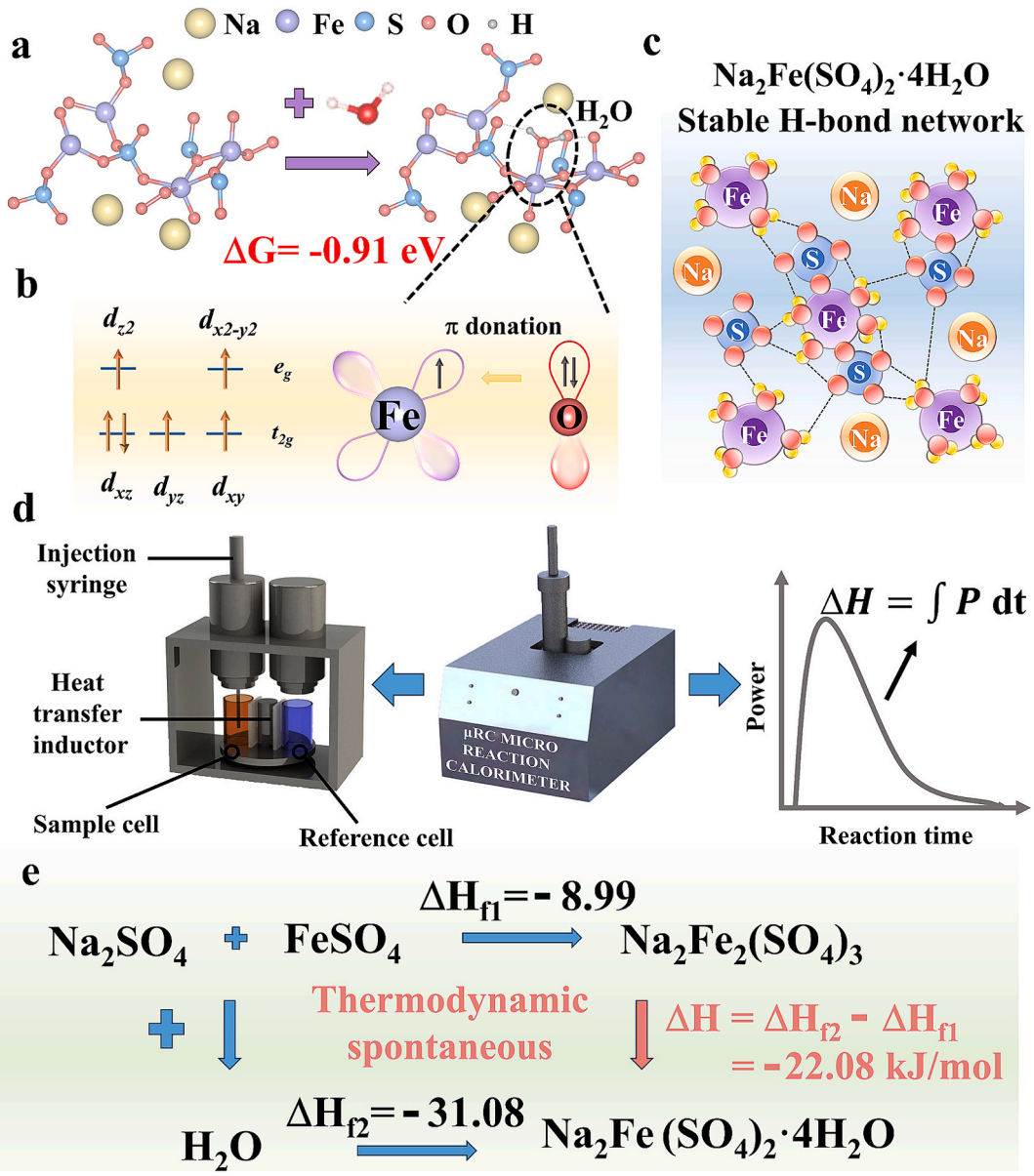

Fig. 3. A) schematic diagram of water adsorption on NFS and the variation of Gibbs free energy. b) Schematic diagram of the electronic coupling mechanism between Fe in NFS and O in water. c) Schematic diagram of the stable hydrogen bond network in $Na_2Fe(SO_4)_2{\cdot}4H_2O$. d) Principle of instrument testing for the μRC Micro-Response Calorimeter. e) Thermodynamic spontaneous cycle of $Na_{2+2x}Fe_{2-x}(SO_4)_3$ to $Na_2Fe(SO_4)_2{\cdot}4H_2O$.

Table 1
Calorimetric data for $Na_{2+2x}Fe_{2-x}(SO_4)_3$ and $Na_2Fe(SO_4)_2{\cdot}4H_2O$.

Substance	ΔH_{ds} (kJ/mol)	ΔH_f (kJ/mol)
Na_2SO_4	12.27	
$FeSO_4$	−9.316	
H_2O	−0.54	
$Na_{2+2x}Fe_{2-x}(SO_4)_3$	2.633	−8.997
$Na_2Fe(SO_4)_2{\cdot}4H_2O$	31.87	−31.08
$Na_2Fe_2(SO_4)_3 + 4H_2O \rightarrow Na_2Fe(SO_4)_2{\cdot}4H_2O + FeSO_4$ ΔH = −22.083		

I_G ratio over time, indicating a decrease in the degree of graphitization (Fig. 4**b and S10b**) [36,37]. The phenomenon arises from the formation of hydrates on the surface of the particles upon water absorption, which interferes with the conductive network of CNTs, resulting in a decline in electronic conductivity. The comparison of the electronic conductivity of NFS in **Table S14** and Fig. 4**d** further illustrates that the conductivity decreases with storage time growth. With the extension of storage time, the weight gain rate of NFS progressively increases (Fig. 4**e**) and the surface morphology of NFS converts from smooth spherical shapes to rough structures owing to volume expansion caused by water adsorption (Fig. 4**c**). As the content of impurities ascents, the likelihood of impurity particles coming into contact and fusion significantly rises, leading to the agglomeration of material particles (**Fig. S10d**), which reflects in a notable drop in specific surface area from 7.06 m^2/g to 1.15 m^2/g (**Fig. S10c**). Characterization results show that water accumulation on the NFS surface leads to a decrease in the material electronic conductivity and causes particle agglomeration.

In addition, we correlate the electrochemical performance with storage time. A hydrated phase content of 31.7 % exists in NFS stored for 48 h, corresponding to a reduction in discharge specific capacity from 103 mAh/g to 86 mAh/g at 0.1C, along with a decline in rate performance (Fig. 4**f-g and Fig. S11a**). As shown in Fig. 4**h** and the detail EIS fitting results in **Table S15**, the interfacial charge transfer resistance (R_{ct}) demonstrates a significant increase from 1020 Ω to 1291 Ω. This is ascribed to the deterioration in the electronic conductivity of the active

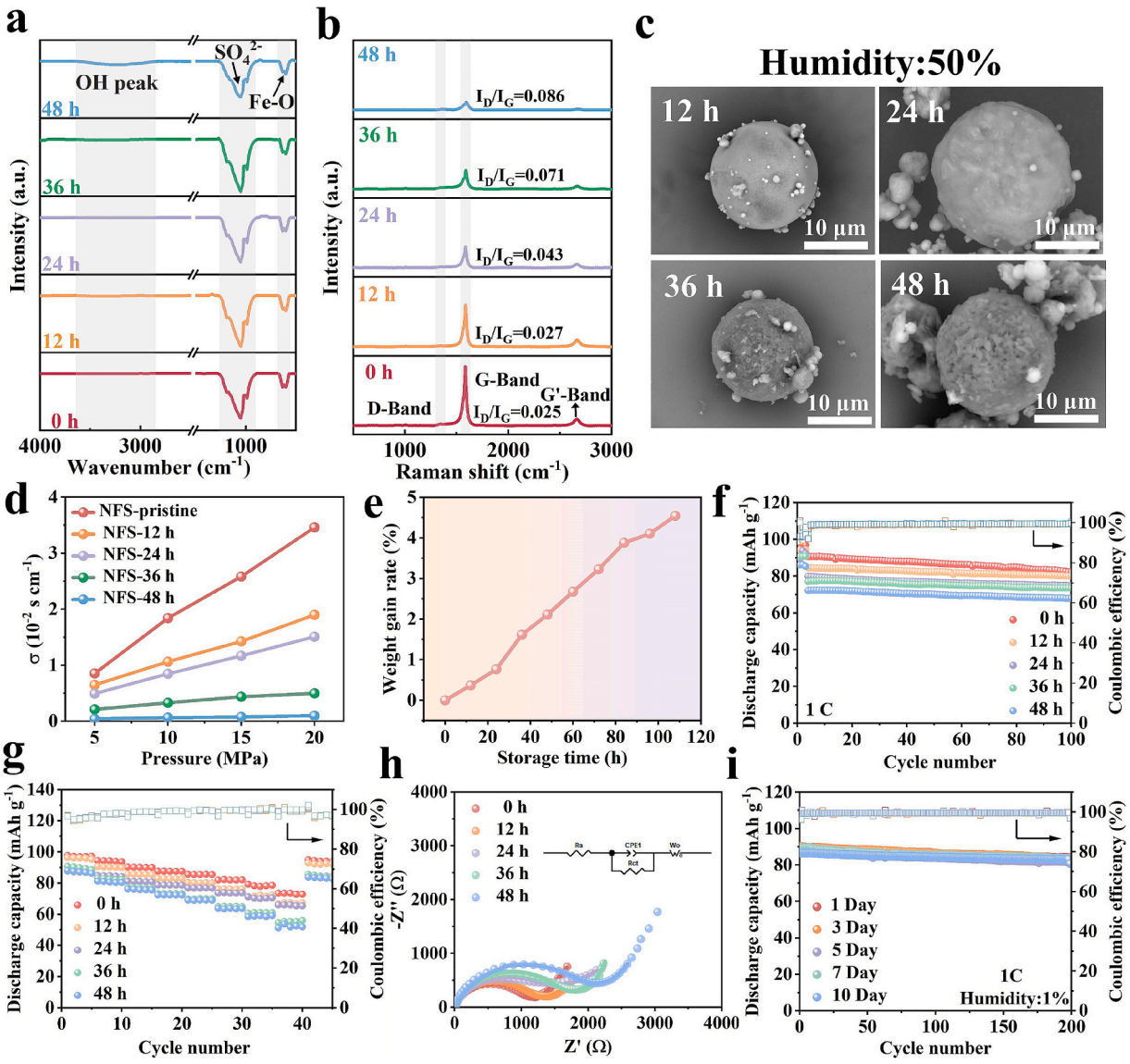

Fig. 4. Changes of NFS over different storage time at 50 % humidity of a) FT-IR spectra, b) Raman spectra, c) SEM images, d) electronic conductivity curves, e) the weight gain rate, f) cycling performance test results at 1C, g) rate performance test results and h) EIS test results. i) Cycle stability tests at 1C of NFS after 1–10 days stored in the dry room (humidity:1%).

particles, which impairs the charge transfer capability and hinders the reversible storage of Na^+. After the entire moisture-induced transformation, the NFS exhibits a discharge specific capacity of only 61.2 mAh/g (**Fig. S11b**) and a redox peak at probable 3.3 V (**Fig. S11c**) consistent with the $Na_2Fe(SO_4)_2{\cdot}4H_2O$ reported in the literature [38]. The degradation in electrochemical performance is primarily derived from the phase transformation. Although $Na_2Fe(SO_4)_2{\cdot}4H_2O$ behaves electrochemical activity, its larger molecular weight results in a milder capacity performance (theoretical specific capacity of 73 mAh/g). Furthermore, to confirm whether the degradation of NFS is entirely induced by moisture, we store the NFS in a dry room (dew point of −60 °C) for XRD and electrochemical performance tests (**Fig. 4i and Fig. S12a-b**). Even after 10 days in the dry room, there is no apparent difference in the XRD patterns or electrochemical performance of NFS, confirming that moisture is the determining factor in inducing material deterioration.

The XRD pattern indicates that the precursor obtained via spray drying consists of $Na_2Fe(SO_4)_2{\cdot}4H_2O$, $Na_2Fe(SO_4)_2{\cdot}H_2O$ and $FeSO_4{\cdot}H_2O$ and the target product is formed after annealing (**Fig. S13a-b**), suggesting that alluaudite $Na_{2+2x}Fe_{2-x}(SO_4)_3$ and bloedite $Na_2Fe(SO_4)_2{\cdot}4H_2O$ materials undergo reversible reactions. Therefore, a simple secondary-heated strategy is proposed to actuate the hydrated $Na_2Fe(SO_4)_2{\cdot}4H_2O$ back to its original crystal phase. The initial, fully water-absorbed, and secondary-heated materials are named NFS-pristine, NFS-wet, and NFS-heat, respectively. We explore the impact of heating temperature on the material composition and performance. The TG curve of NFS-wet is exhibited in **Fig. S14a**, where no significant weight loss occurs above 350 °C. Additionally, XRD and electrochemical results indicate that conspicuous presence of impurities at the heating temperature of 250 °C and 300 °C triggers to inferior electrochemical performance (**Fig. S14b-c**). Thus, 350 °C is selected as the optimal heating temperature. Fig. 5**a** demonstrates the comparison of NFS-pristine, NFS-wet, and NFS-heat in XRD patterns, indicating the NFS-heat reconstructs to alluaudite-type crystal structure with acceptable purity. After heating, the surface becomes relatively smooth and porous as the escape of internal crystalline water (Fig. 5**b**), resulting in an improvement in the specific surface area to 15.8 m^2/g (**Fig. S15**).

Further analysis of the elemental composition after hydration and heating is conducted through XPS. Regarding the S 2p spectra, the peaks at 168.6 eV (S $2p^{3/2}$) and 169.8 eV (S $2p^{1/2}$) are assigned to the SO_4

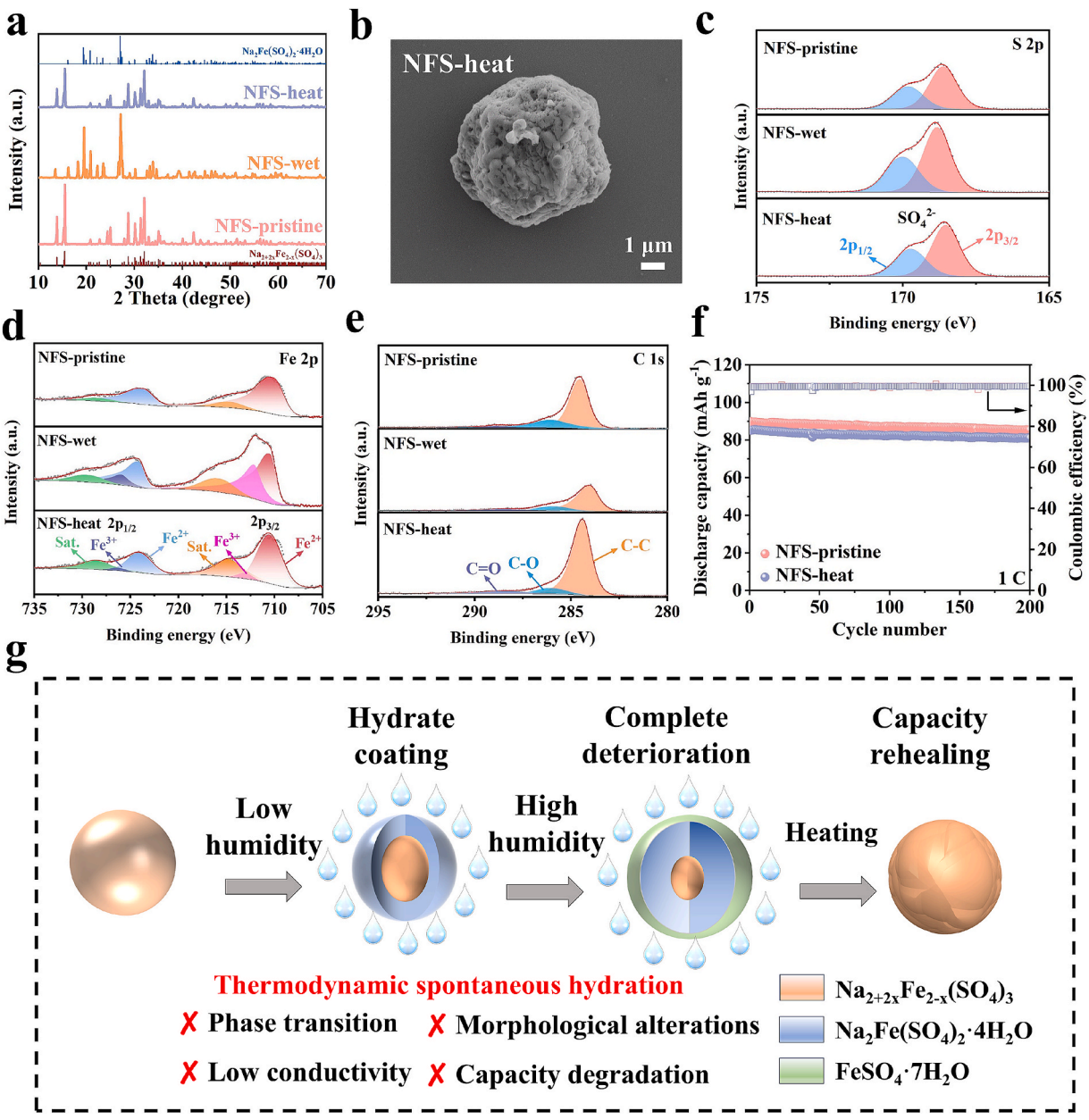

Fig. 5. A) Comparison of XRD spectra of NFS-pristine, NFS-wet, and NFS-heat. b) SEM image of NFS-heat. XPS spectra of NFS-pristine, NFS-wet, and NFS-heat c) S 2p, d) Fe 2p, e) C 1 s. f) Cycling stability tests of NFS-pristine and NFS-heat. g) Diagram of the process for moisture-induced degradation of $Na_{2+2x}Fe_{2-x}(SO_4)_3$ to $Na_2Fe(SO_4)_2·4H_2O$.

group, and the S content shows an upward trend of NFS-wet, attributed to the surface precipitation of $FeSO_4·7H_2O$ impurities (Fig. 5**c**) [39,40]. The intensity of the O-H peak at 535.9 eV in the O 1 s spectra of NFS-wet is significantly enhanced, indicating the material's water adsorption (**Fig. S16a**). In NFS-pristine, the valence of Fe is confirmed to be + 2 by the peaks at 710.5 eV (Fe $2p^{3/2}$) and 724.2 eV (Fe $2p^{1/2}$) in the Fe 2p spectrum [41]. After storage, peaks are observed at 712.3 eV and 725.9 eV in NFS-wet, suggesting that fractional Fe^{2+} is oxidized to Fe^{3+} after hydration [42,43]. Fortunately, partial reduction of Fe^{3+} back to Fe^{2+} occurs in NFS-heat during heating under a reducing Ar-H_2 atmosphere as indicated by the significant reduction in the intensity of the peak associated with Fe^{3+} (Fig. 5**d**). The loss of this electrochemically active redox pair explains the decline in electrochemical performance after hydration. The C spectra of the NFS at 284.4, 286.0, and 288.3 eV correspond to C–C, C–O, and C=O, representing typical functional groups of conductive carbon, which are intimately associated with the charge transfer processes and electronic conductivity (Fig. 5**e**) [44]. The peak intensity weakens after hydration and enhances after heating, correlating exactly with the decline and subsequent rise in the material conductivity (**Fig. S16b**).

NFS-heat reveals a marginally lower I_D/I_G in Raman spectra and a mildly higher impedance R_{ct} than that of NFS-pristine owing to a destruction in the conductive network of CNTs leading to reduced electronic conductivity (**Fig. S17a-b**). The Na^+ transport kinetics of the NFS-heat is improved, with a slight growth in the Na^+ diffusion coefficient compared to the NFS-pristine, as observed in the GITT test (**Fig. S17c**). This is because the incremental specific surface area enhances ion adsorption and diffusion on the material surface. Subsequently, the electrochemical performance of the NFS-heat is evaluated, showing a discharge capacity of 85.7 mAh/g at 1C and 97 mAh/g at 0.1C recovered 94 % of NFS-pristine (Fig. 5**f and Fig. S17d-e**). This irreversible capacity loss results from the incomplete phase transformation,

partial damage of the electrochemically active redox pair and diminishing electronic conductivity. NFS-heat manifests stable cycling, with a capacity retention of 82.7 % after 1000 cycles at 1C, suggesting that the secondary-heated strategy effectively recovers the rigid structural framework of the degraded material (**Fig. S17f**).

The process for moisture-induced degradation and secondary heating rehealing of NFS is shown in Fig. 5**g**. When $Na_{2+2x}Fe_{2-x}(SO_4)_3$ is exposed to a humid environment, water first adsorb into the pore structure of the material, and then penetrate into the crystal lattice. The entry of water molecules causes partial substitution of SO_4^{2-} by H_2O and $[Fe_2O_{10}]$ altering to $[FeO_6]$, forming a new hydrated phase $Na_2Fe(SO_4)_2{\cdot}4H_2O$. This transformation is thermodynamically driven, meaning that the hydration process lowers the system energy and forms a more stable phase. In high-humidity environments, the hydration process intensifies, further promoting the formation of $FeSO_4{\cdot}7H_2O$. The material undergoes a phase transition, accompanied by a decrease in conductivity and changes in morphology, which significantly degrades the electrochemical performance. After secondary heating, the water molecules are gradually released, and the dehydrated bloedite-type material undergoes ion redistribution and lattice contraction, ultimately reconstructing the alluaudite-type structure and recovering the capacity.

3. Conclusion

In summary, we conduct $Na_{2.67}Fe_{1.67}(SO_4)_3$ coated by CNTs through the spray-drying method with an initial capacity of 103 mAh/g and a capacity retention of 77.8 % after 6000 cycles at 10 C. Subsequently, as-synthesized NFS is used as a model to investigate the intrinsic causes of air instability and systematically evaluate the changes in crystal structure, system energy, chemical composition, and electrochemical performance. In detail, after the NFS material is exposed to 50 % humidity for 2 days, the 31.7 % $Na_2Fe(SO_4)_2{\cdot}4H_2O$ impurity formation is detected. Upon exposure to moisture, water adsorbs around the Fe atoms and forms hydrogen-bonding network with the oxygen atoms in the lattice, thereby enhancing the structural stability. Additionally, the strong Coulombic repulsion between Fe atoms causes the $[Fe_2O_{10}]$ dimers to transform into $[FeO_6]$ octahedra, leading to the formation of a bloedite-type $Na_2Fe(SO_4)_2{\cdot}4H_2O$. The enthalpy change of the hydration reaction is –22.083 kJ/mol and theoretical calculations suggest that ΔG of the reaction is −0.91 eV, indicating that the moisture-induced phase transition of NFS is thermodynamically spontaneous. After water absorption, the NFS material undergoes the following changes: (i) The crystalline phase is replaced by the milder capacity-wise bloedite-type hydrated phase $Na_2Fe(SO_4)_2{\cdot}4H_2O$. (ii) The morphology of NFS transforms from smooth spheres to a rough structure, with visible impurities clearly appearing on the surface. (iii) Fe^{2+} is oxidized to Fe^{3+} causing the loss of active electrochemical pairs. (iv) Electronic conductivity declines significantly, all of which ultimately lead to deterioration of electrochemical performance. After full hydration, the discharge capacity of NFS decreases to 61.2 mAh/g and then following secondary heating, the capacity can be recovered to 97 mAh/g, which is 94 % of the initial value. This partial irreversible capacity loss is due to the disruption of active electrochemical pairs and conductivity, which limits the reversible storage of sodium ions. This work provides a comprehensive explanation of the moisture-induced degradation of $Na_{2+2x}Fe_{2-x}(SO_4)_3$ and offers a systematic evaluation of how structural transitions, morphological changes, and physicochemical properties during humidity-induced degradation affect electrochemical performance.

CRediT authorship contribution statement

Jiayue Wu: Writing – original draft, Software, Methodology, Investigation, Formal analysis, Data curation, Conceptualization. **Xing Chen:** Writing – review & editing, Data curation. **Jing Zeng:** Writing – review & editing, Supervision, Project administration, Funding acquisition. **Jinbao Zhao:** Writing – review & editing, Resources, Project administration, Funding acquisition.

Declaration of competing interest

The authors declare that they have no known competing financial interests or personal relationships that could have appeared to influence the work reported in this paper.

Acknowledgments

The authors gratefully acknowledge the National Natural Science Foundation of China (Nos. 21875198, 22005257, and 22021001), Natural Science Foundation of Fujian Province of China (No.2020 J05009) and NFFTBS No. J1310024 for financial support. We are grateful to Dr. Yuhao Hong at Tan Kah Kee Innovation Laboratory (IKKEM), Center for Micro-nano Fabrication and Advanced Characterization, Xiamen University for help with the XPS measurement.

Appendix A. Supplementary data

Supplementary data to this article can be found online at https://doi.org/10.1016/j.cej.2025.162535.

Data availability

Data will be made available on request.

References

[1] V. Viswanathan, A. Epstein, Y. Chiang, E. Takeuchi, M. Bradley, J. Langford, M. Winter, The challenges and opportunities of battery-powered flight, Nature 601 (7894) (2022) 519–525, https://doi.org/10.1038/s41586-021-04139-1.
[2] Q. Wei, X. Chang, J. Wang, T. Huang, X. Huang, J. Yu, H. Zheng, J. Chen, D. Peng, An ultrahigh-power mesocarbon microbeads|Na^+-diglyme|$Na_3V_2(PO_4)_3$ sodium-Ion battery, Adv. Mater. 34 (6) (2022) 2108304, https://doi.org/10.1002/adma.202108304.
[3] P. Li, S. Luo, Y. Lin, J. Xiao, X. Xia, X. Liu, L. Wang, X. He, Fundamentals of the recycling of spent lithium-ion batteries, Chem. Soc. Rev. 53 (24) (2024) 11967–12013, https://doi.org/10.1039/D4CS00362D.
[4] Y. Ha, S. Roh, B. Park, M. Kim, D. Jeong, H. Kim, I. Kim, Y. Jo, J. Choi, K. Kim, Innovative fast-charging protocol incorporating proactive lithium-plating suppression pulses for lithium-Iion batteries: protocol design, validation, and post-mortem analysis, Adv. Energy Mater. 2402032 (2024), https://doi.org/10.1002/aenm.202402032.
[5] P. Li, T. Yuan, J. Qiu, H. Che, Q. Ma, Y. Pang, Z. Ma, S. Zheng, A comprehensive review of layered transition metal oxide cathodes for sodium-ion batteries: The latest advancements and future perspectives, Mat. Sci. Eng. r. 163 (2025) 100902, https://doi.org/10.1016/j.mser.2024.100902.
[6] Y. Yu, J. Zhang, R. Gao, D. Wong, K. An, L. Zheng, N. Zhang, C. Schulz, X. Liu, Triggering reversible anion redox chemistry in O3-type cathodes by tuning Na/Mn anti-site defects, Energy Environ. Sci. 16 (2) (2023) 584–597, https://doi.org/10.1039/D2EE03874A.
[7] Y. Wu, W. Shuang, Y. Wang, F. Chen, S. Tang, X. Wu, Z. Bai, L. Yang, J. Zhang, Recent progress in sodium-ion batteries: advanced materials, reaction mechanisms and energy applications, Electrochem. Energy Rev. 7 (2024) 17, https://doi.org/10.1007/s41918-024-00215-y.
[8] K. Mathiyalagan, R. Raja, D. Shin, Y. Lee, Research progress in sodium-iron-phosphate-based cathode materials for cost-effective sodium-ion batteries: Crystal structure, preparation, challenges, strategies, and developments, Prog. Mater. Sci. 151 (2025) 101425, https://doi.org/10.1016/j.pmatsci.2024.101425.
[9] Z. Zheng, Y. Wang, Y. Zhang, X. Li, Y. Zhang, Y. He, H. Che, L. Li, Z. Ma, Sodium iron sulfate cathodes with ultra-long cycle-life and high safety for sodium-ion batteries, Nano Energy 128 (2024) 109907, https://doi.org/10.1016/j.nanoen.2024.109907.
[10] X. Lu, S. Li, Y. Li, F. Wu, C. Wu, Y. Bai, From lab to application: challenges and opportunities in achieving fast charging with polyanionic cathodes for sodium-ion batteries, Adv. Mater. 36 (2024) 2407359, https://doi.org/10.1002/adma.202407359.
[11] Z. Fan, W. Song, N. Yang, C. Lou, R. Tian, W. Hua, M. Tang, F. Du, Insights into the phase purity and storage mechanism of nonstoichiometric $Na_{3.4}Fe_{2.4}(PO_4)_{1.4}P_2O_7$ cathode for high-mass-loading and high-power-density sodium-ion batteries, Angew. Chem. Int. Ed. 63 (8) (2024) e202316957, https://doi.org/10.1002/anie.202316957.
[12] Z. Ahsan, Z. Cai, S. Wang, M. Moin, H. Wang, D. Liu, Y. Ma, G. Song, C. Wen, Recent development of phosphate based polyanion cathode materials for sodium-

ion batteries, Adv. Energy Mater. 14 (2024) 2400373, https://doi.org/10.1002/aenm.202400373.
[13] Y. Liu, Y. Han, Z. Song, W. Song, Z. Miao, Y. Chen, J. Ding, W. Hu, Accelerating the phase formation kinetics of alluaudite sodium iron sulfate cathodes via ultrafast thermal shock, ACS Appl. Mater. Interfaces. 16 (11) (2024) 13828–13838, https://doi.org/10.1021/acsami.3c19618.
[14] P. Barpanda, G. Oyama, S. Nishimura, S. Chung, A. Yamada, A,, 3.8-V earth-abundant sodium battery electrode, Nat. Commun. 5 (1) (2014) 4358, https://doi.org/10.1038/ncomms5358.
[15] J. Zhang, Y. Yan, X. Wang, Y. Cui, Z. Zhang, S. Wang, Z. Xie, P. Yan, W. Chen, Bridging multiscale interfaces for developing ionically conductive high-voltage iron sulfate-containing sodium-based battery positive electrodes, Nat. Commun. 14 (1) (2023) 3701, https://doi.org/10.1038/s41467-023-39384-7.
[16] X. Xiao, Y. Lan, L. Tan, H. Xu, W. Yao, Y. Tang, Alluaudite $Na_2Fe_2(SO_4)_3$ and NASICON-type $Na_4Fe_3(PO_4)_2(P_2O_7)$ as promising cathode materials in sodium-ion batteries, Adv. Funct. Mater. 34 (2024) 2411280, https://doi.org/10.1002/adfm.202411280.
[17] Z. Gu, X. Zhao, K. Li, J. Cao, X. Wang, J. Guo, H. Liu, S. Zheng, D. Liu, H. Wu, X. Wu, Homeostatic solid solution reaction in phosphate cathode: breaking high-voltage barrier to achieve high energy density and long life of sodium-ion batteries, Adv. Mater. 36 (2024) 2400690, https://doi.org/10.1002/adma.202400690.
[18] L. Deng, Y. Zhang, Y. Tang, Y. Li, W. Ma, L. Liu, S. Dong, Y. Cao, Carbon coated Fe-based sulphate nanoparticles within continuous conductive network for low-cost and high-performance symmetrical sodium-ion batteries, Adv. Funct. Mater. 34 (2024) 2402145, https://doi.org/10.1002/adfm.202402145.
[19] S. Singh, P. Jha, M. Avdeev, W. Zhang, K. Jayanthi, A. Navrotsky, H. Alshareef, P. Barpanda, Marinite $Li_2Ni(SO_4)_2$ as a new member of the bisulfate family of high-voltage lithium battery cathodes, Chem. Mater. 33 (15) (2021) 6108–6119, https://doi.org/10.1021/acs.chemmater.1c01669.
[20] L. Zhang, J. Tarascon, M. Sougrati, G. Rousse, G. Chen, Influence of relative humidity on the structure and electrochemical performance of sustainable $LiFeSO_4F$ electrodes for Li-ion batteries, J. Mater. Chem. a. 3 (33) (2015) 16988–16997, https://doi.org/10.1039/C5TA05107J.
[21] C. Liu, K. Chen, F. Li, A. Zhao, Z. Chen, Y. Fang, Y. Cao, Anion-doped $Na_{2.9}Fe_{1.7}(SO_4)_{2.7}(PO_4)_{0.3}$ cathode with improved cyclability and air stability for low-cost sodium-ion batteries, Nano Energy 125 (2024) 109557, https://doi.org/10.1016/j.nanoen.2024.109557.
[22] Y. Meng, Q. Li, T. Yu, S. Zhang, C. Deng, Architecture–property relationships of zero-, one- and two-dimensional carbon matrix incorporated $Na_2Fe(SO4)_2{\cdot}2H_2O$/C, CrstEngComm 18 (9) (2016) 1645–1654, https://doi.org/10.1039/C5CE02046H.
[23] Y. Meng, S. Zhang, C. Deng, Superior sodium–lithium intercalation and depressed moisture sensitivity of a hierarchical sandwich-type nanostructure for a graphene–sulfate composite: a case study on $Na_2Fe(SO_4)_2{\cdot}2H_2O$, J. Mater. Chem. a. 3 (8) (2015) 4484–4492, https://doi.org/10.1039/C4TA06711H.
[24] W. Yang, Q. Liu, Q. Yang, X. Zhang, Z. Yang, D. Mu, L. Li, R. Chen, F. Wu, Uncovering the nonequilibrium evolution mechanism between $Na_{2+2\delta}Fe_{2-\delta}(SO_4)_3$ cathode and impurities in the Na_2SO_4-$FeSO_4{\cdot}7H_2O$ binary system for high-voltage sodium-ion batteries, Small 20 (2024) 2405982, https://doi.org/10.1002/smll.202405982.
[25] W. Yang, Q. Liu, Q. Yang, S. Lu, W. He, L. Li, R. Chen, F. Wu, Transitioning from anhydrous Stanfieldite-type $Na_2Fe(SO_4)_2$ precursor to Alluaudite-type $Na_{2+2\delta}Fe_{2-\delta}(SO_4)_3$/C composite cathode: A pathway to cost-effective and all-climate sodium-ion batteries, Energy Stor. Mater. 74 (2025) 103925, https://doi.org/10.1016/j.ensm.2024.103925.
[26] J. Hou, S. Chen, W. Wang, K. Wang, K. Jiang, Electrochemical lithium storage mechanism exploration of a 4.1 V cathode material with high energy/power density and low cost, Chem. Eng. J. 470 (2023) 144159, https://doi.org/10.1016/j.cej.2023.144159.
[27] Q. Xiao, Y. Li, K. Wang, C. Ma, B. Liu, Y. Zhao, Flash graphene induced low-temperature synthesis of a single-crystalline $Na_{2.72}Fe_{1.64}(SO_4)_3$ cathode for boosted sodium storage, J. Mater. Chem. a. (2025), https://doi.org/10.1039/D4TA07478E.
[28] X. Pu, D. Zhao, C. Fu, Z. Chen, S. Cao, C. Wang, Y. Cao, Understanding and calibration of charge storage mechanism in cyclic voltammetry curves, Angew. Chem. Int. Ed. 60 (39) (2021) 21310–21318, https://doi.org/10.1002/anie.202104167.
[29] Z. Zheng, X. Li, Y. Wang, Y. Zhang, Y. Jiang, Y. He, C. Niu, H. Che, L. Li, Z. Ma, Self-limited and reversible surface hydration of $Na_2Fe(SO_4)_2$ cathodes for long-cycle-life Na-ion batteries, Energy Stor. Mater. 74 (2025) 103882, https://doi.org/10.1016/j.ensm.2024.103882.
[30] A. Radha, L. Lander, G. Rousse, J. Tarascon, A. Navrotsky, Thermodynamic stability and correlation with synthesis conditions, structure and phase transformations in orthorhombic and monoclinic $Li_2M(SO_4)_2$ (M = Mn, Fe, Co, Ni) polymorphs, J. Mater. Chem. A 3 (6) (2015) 2601–2608, https://doi.org/10.1039/C4TA05066E.
[31] S. Zones, K. Jayanthi, J. Pascual, D. Xie, A. Navrotsky, Energetics of the local environment of structure-directing agents influence zeolite synthesis, Chem. Mater. 33 (6) (2021) 2126–2138, https://doi.org/10.1021/acs.chemmater.0c04796.
[32] W. Dang, W. Guo, W. Chen, J. Wang, Q. Zhang, Extreme environment-adaptable and ultralong-life energy storage enabled by synergistic manipulation of interfacial environment and hydrogen bonding, Energy Stor. Mater. 74 (2025) 103915, https://doi.org/10.1016/j.ensm.2024.103915.
[33] Y. Liu, R. Rajagopalan, E. Wang, M. Chen, W. Hua, B. Zhong, Y. Zhong, Z. Wu, X. Guo, Insight into the multirole of graphene in preparation of high performance $Na_{2+2x}Fe_{2-x}(SO_4)_3$ cathodes, ACS Sustainable Chem. Eng. 6 (12) (2018) 16105–16112, https://doi.org/10.1021/acssuschemeng.8b02679.
[34] M. Chen, D. Cortie, Z. Hu, H. Jin, S. Wang, Q. Gu, W. Hua, E. Wang, W. Lai, L. Chen, S. Chou, X. Wang, S. Dou, A novel graphene oxide wrapped $Na_2Fe_2(SO_4)_3$/C cathode composite for long life and high energy density sodium-ion batteries, Adv. Energy Mater. 8 (2018) 1800944, https://doi.org/10.1002/aenm.201800944.
[35] W. Yang, Q. Liu, L. Hou, Q. Yang, D. Mu, G. Tan, L. Li, R. Chen, F. Wu, Spherical shell with CNTs network structuring Fe-based Alluaudite $Na_{2+2\delta}Fe_{2-\delta}(SO_4)_3$ cathode and novel phase transition mechanism for sodium-ion battery, Small 20 (2024) 2306595, https://doi.org/10.1002/smll.202306595.
[36] J. Hou, W. Wang, P. Feng, K. Wang, K. Jiang, A surface chemistry assistant strategy to high power/energy density and cost-effective cathode for sodium ion battery, J. Power Sources 453 (2020) 227879, https://doi.org/10.1016/j.jpowsour.2020.227879.
[37] Y. Fang, Q. Liu, X. Feng, W. Chen, X. Ai, L. Wang, L. Wang, Z. Ma, Y. Ren, H. Yang, Y. Cao, An advanced low-cost cathode composed of graphene-coated $Na_{2.4}Fe_{1.8}(SO_4)_3$ nanograins in a 3D graphene network for ultra-stable sodium storage, J. Energy Chem. 54 (2021) 564–570, https://doi.org/10.1016/j.jechem.2020.06.020.
[38] M. Reynaud, M. Ati, S. Boulineau, M. Sougrati, B. Melot, G. Rousse, J. Chotard, J. Tarascon, Bimetallic sulfates $A_2M(SO_4)_2{\cdot}nH_2O$ (A = Li, Na and M = Transition Metal): as new attractive electrode materials for Li- and Na-Ion batteries, ECS Trans. 50 (24) (2013) 11, https://doi.org/10.1149/05024.0011ecst.
[39] S. Li, X. Song, X. Kuai, W. Zhu, K. Tian, X. Li, M. Chen, S. Chou, J. Zhao, L. Gao, A nanoarchitectured $Na_6Fe_5(SO_4)_8$/CNTs cathode for building a low-cost 3.6 V sodium-ion full battery with superior sodium storage, J. Mater. Chem. A 7 (24) (2019) 14656–14669, https://doi.org/10.1039/C9TA03089A.
[40] X. Hu, J. Jia, G. Wang, J. Chen, H. Zhan, Z. Wen, Reliable and general route to inverse opal structured nanohybrids of carbon-confined transition metal sulfides quantum dots for high-performance sodium storage, Adv. Energy Mater. 8 (25) (2018) 1801452, https://doi.org/10.1002/aenm.201801452.
[41] P. Singh, K. Shiva, H. Celio, J. Goodenough, Eldfellite, $NaFe(SO_4)_2$: an intercalation cathode host for low-cost Na-ion batteries, Energy Environ. Sci. 8 (10) (2015) 3000–3005, https://doi.org/10.1039/C5EE02274F.
[42] S. Pinjari, R. Dutta, S. Parshanaboina, P. Mudavath, S. Singha, D. Dubal, X. Wang, J. Bell, A. Nanjundan, R. Gaddam, Multivalent cation substitution boosted sodium-ion storage in NASICON-type iron-phospho-sulphate cathodes, Chem. Eng. J. 502 (2024) 157979, https://doi.org/10.1016/j.cej.2024.157979.
[43] T. Yamashita, P. Hayes, Analysis of XPS spectra of Fe^{2+} and Fe^{3+} ions in oxide materials, Appl. Surf. Sci. 254 (8) (2008) 2441–2449, https://doi.org/10.1016/j.apsusc.2007.09.063.
[44] M. Guo, J. Wang, H. Dou, G. Gao, S. Wang, J. Wang, Z. Xiao, G. Wu, X. Yang, Z. Ma, Agglomeration-resistant 2D nanoflakes configured with super electronic networks for extraordinary fast and stable sodium-ion storage, Nano Energy 56 (2019) 502–511, https://doi.org/10.1016/j.nanoen.2018.11.091.